

Fluid–solid interactions: modeling, simulation, bio-mechanical applications

# A two-dimensional effective model describing fluid–structure interaction in blood flow: analysis, simulation and experimental validation

Sunčica Čanić<sup>a,1</sup>, Andro Mikelić<sup>b,\*</sup>, Josip Tambača<sup>c</sup>

<sup>a</sup> Department of Mathematics, University of Houston, 4800 Calhoun Rd., Houston, TX 77204-3476, USA

<sup>b</sup> Institut Camille Jordan, UFR mathématiques, site de Gerland, bâtiment. A, université Claude–Bernard Lyon 1, 50, avenue Tony Garnier, 69366 Lyon cedex 07, France

<sup>c</sup> Department of Mathematics, University of Zagreb, Bijenička 30, 10000 Zagreb, Croatia

Available online 17 November 2005

## Abstract

We derive a closed system of effective equations describing a time-dependent flow of a viscous incompressible Newtonian fluid through a long and narrow elastic tube. The 3D axially symmetric incompressible Navier–Stokes equations are used to model the flow. Two models are used to describe the tube wall: the linear membrane shell model and the linearly elastic membrane and the curved, linearly elastic Koiter shell model. We study the behavior of the coupled fluid–structure interaction problem in the limit when the ratio between the radius and the length of the tube,  $\varepsilon$ , tends to zero. We obtain the reduced equations that are of Biot type with memory. An interesting feature of the reduced equations is that the memory term explicitly captures the viscoelastic nature of the coupled problem. Our model provides significant improvement over the standard 1D approximations of the fluid–structure interaction problem, all of which assume an ad hoc closure assumption for the velocity profile. We performed experimental validation of the reduced model using a mock circulatory flow loop assembled at the Cardiovascular Research Laboratory at the Texas Heart Institute. Experimental results show excellent agreement with the numerically calculated solution. Major applications include blood flow through large human arteries. *To cite this article: S. Čanić et al., C. R. Mecanique 333 (2005).*

© 2005 Académie des sciences. Published by Elsevier SAS. All rights reserved.

## Résumé

**Un modèle efficace bidimensionnel décrivant l'interaction fluide–structure dans l'écoulement sanguin : analyse, simulation et validation expérimentale.** Nous obtenons un système fermé d'équations efficaces, décrivant l'écoulement non-stationnaire d'un fluide newtonien incompressible visqueux à travers un tuyau élastique long et de faible épaisseur. Pour modéliser l'écoulement, nous utilisons le système de Navier–Stokes 3D axisymétrique et incompressible. Deux modèles sont employés pour décrire le comportement élastique de la paroi latérale : les équations de Navier pour une membrane courbe élastique linéaire, et ensuite le modèle de Koiter, d'une coque courbe, élastique linéaire. Nous étudions le comportement du système lorsque le rapport  $\varepsilon$ , entre l'épaisseur caractéristique et la longueur du tube, tend vers zéro. Nous obtenons les équations efficaces, essentiellement 1D, qui sont du type de Biot avec mémoire. Une caractéristique intéressante des équations efficaces est que le terme de mémoire capture explicitement la nature viscoélastique du problème couplé. Notre modèle efficace fournit une amélioration significative par rapport

\* Corresponding author.

E-mail addresses: [canic@math.uh.edu](mailto:canic@math.uh.edu) (S. Čanić), [mikelic@univ-lyon1.fr](mailto:mikelic@univ-lyon1.fr) (A. Mikelić), [tambaca@math.hr](mailto:tambaca@math.hr) (J. Tambača).

<sup>1</sup> This research was supported by the Texas Higher Education Board, ARP grant #003652-0112-2001 and by the National Science Foundation under grants DMS9970310 and DMS0245513.

aux modèles 1D standards de l'interaction fluide–structure, qui nécessitent une formule de fermeture pour la vitesse, proposée ad hoc. Nous avons effectué la validation expérimentale du modèle réduit en utilisant la boucle d'écoulement simulé au Cardiovascular Research Laboratory, Texas Heart Institute. Les résultats expérimentaux montrent un accord excellent avec la solution calculée numériquement. L'application principale inclut l'écoulement sanguin à travers les grandes artères du corps humain. **Pour citer cet article** : S. Čanić et al., C. R. Mécanique 333 (2005).

© 2005 Académie des sciences. Published by Elsevier SAS. All rights reserved.

*Keywords*: Computational fluid mechanics; Blood flow; Asymptotic methods; Fluid–structure interaction; 3D Navier–Stokes equations

*Mots-clés* : Mécanique des fluides numérique ; Écoulements sanguin ; Méthodes asymptotiques ; Interaction fluide–structure ; Système de Navier–Stokes 3D

## 1. Introduction

This work is motivated by the study of blood flow in compliant arteries. In medium to large vessels such as the human aorta and iliac arteries, blood can be modeled as a viscous, incompressible Newtonian fluid, [1,2]. Driven by a time-periodic pressure pulse caused by the contractions and relaxations of the heart muscle, blood flow interacts with the pulsation of arteries. Modeling and simulation of the fluid–structure interaction between blood flow and arterial walls have been studied by many authors, see, for example, [3–8,1]. However, real-time calculations of large sections of the vascular system are still out of reach. Simplified models need to be used whenever possible. In axially symmetric sections of the vascular system one-dimensional models have been used to speed up the simulation, [9–11,5, 12,8,1]. These models have two drawbacks: they are not closed (an ad hoc assumption needs to be made on the shape of the axial velocity profile to close the system) and outflow boundary conditions generate nonphysiological reflected waves that contaminate the flow. The latter is due to the fact that the system is hyperbolic and Dirichlet boundary conditions give rise to the reflections from the artificially posed outlet boundary that are of the same magnitude as the physiological waves themselves, see [13,5]. In the present article we derive a simplified, effective model that gets around both drawbacks. The resulting equations are closed (the closure follows from the three-dimensional problem itself), and the nonphysiological reflected waves are minimized by the fact that the model equations are of mixed hyperbolic-parabolic type, with memory. The memory terms explicitly capture the observed viscoelastic nature of the fluid–structure interaction in blood flow. Although the resulting equations are two-dimensional, their simplified form allows a decomposition into a set of coupled one-dimensional problems, thereby allowing numerical simulation with complexity of the one-dimensional problems. In this article we present the derivation of the effective equations, a numerical method for their simulation and experimental validation performed on a mock flow loop at the Cardiovascular Research Laboratory at the Texas Heart Institute. The experimental validation shows excellent agreement with the numerically calculated solution.

## 2. The three-dimensional fluid–structure interaction model

We study the flow of an incompressible, viscous Newtonian fluid through a cylinder with compliant walls. In the reference state the cylinder is  $L > 0$  units long and  $2R > 0$  units wide. The aspect ratio  $\varepsilon := R/L > 0$  is assumed to be small. For a given  $R, L > 0$  denote the reference cylinder by  $\Omega_\varepsilon = \{(r \cos \theta, r \sin \theta, z) \in \mathbb{R}^3 : r \in (0, R), \theta \in (0, 2\pi), z \in (0, L)\}$  and its lateral boundary by  $\Sigma_\varepsilon = \{(R \cos \theta, R \sin \theta, z) \in \mathbb{R}^3 : \theta \in (0, 2\pi), z \in (0, L)\}$ ; see Fig. 1. We study a time-dependent flow driven by the time-dependent inlet and outlet boundary data. The compliant cylinder and its boundary deforms as a result of the fluid–structure interaction between the fluid occupying the domain and the cylinder's boundary.

We assume that the lateral wall of the cylinder behaves as a homogeneous, isentropic, linearly elastic shell of thickness  $h$ . We consider two linearly elastic shell models: the linearly elastic membrane model (1) and the linear Koiter shell model (2), studied in [14–17]. Accounting for only radial displacements  $\eta^\varepsilon(z, t)$  and assuming a prestressed reference configuration at reference pressure  $p_{\text{ref}}$  [18,19], the model equations, in Lagrangian coordinates, take the following form:

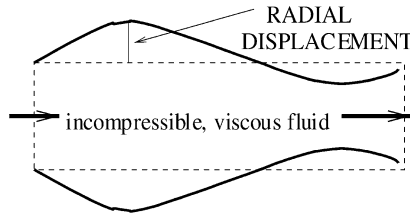


Fig. 1. Domain sketch.

Fig. 1. Visualisation du domaine.

• *The linear membrane model*

$$f_r := \rho_S h \frac{\partial^2 \eta^\epsilon}{\partial t^2} + \frac{hE}{1 - \sigma^2} \frac{1}{R^2} \eta^\epsilon + p_{\text{ref}} \frac{\eta^\epsilon}{R} \tag{1}$$

• *The linear Koiter shell model*

$$f_r = \rho_S h \frac{\partial^2 \eta^\epsilon}{\partial t^2} + \frac{hE}{1 - \sigma^2} \frac{1}{R^2} \eta^\epsilon + \frac{hE}{1 - \sigma^2} \frac{h^2}{12} \left( \frac{\partial^4 \eta^\epsilon}{\partial z^4} - 2 \frac{\sigma}{R^2} \frac{\partial^2 \eta^\epsilon}{\partial z^2} + \frac{1}{R^4} \eta^\epsilon \right) + p_{\text{ref}} \frac{\eta^\epsilon}{R} \tag{2}$$

Here  $E$  is the Young’s modulus,  $\rho_S$  is the shell density,  $\sigma$  is the Poisson ratio and  $f_r$  is the radial component of the contact force.

The fluid is modeled by the incompressible Navier–Stokes equations, defined on the deformed domain  $\Omega_\epsilon(t) = \{(r, \theta, z) \mid r < R + \eta^\epsilon(z, t), \theta \in [0, 2\pi), z \in (0, L)\}$  with the lateral, inlet and outlet boundary  $\Sigma_\epsilon(t) = \{r = R + \eta^\epsilon(z, t), z \in (0, L)\}$ ,  $B_0^\epsilon(t) := \partial\Omega_\epsilon(t) \cap \{z = 0\}$ ,  $B_L^\epsilon(t) := \partial\Omega_\epsilon(t) \cap \{z = L\}$ , respectively. Assuming zero azimuthal velocity, the Eulerian formulation of the equations in cylindrical coordinates reads

$$\rho \left( \frac{\partial v_r^\epsilon}{\partial t} + v_r^\epsilon \frac{\partial v_r^\epsilon}{\partial r} + v_z^\epsilon \frac{\partial v_r^\epsilon}{\partial z} \right) - \mu \left( \frac{\partial^2 v_r^\epsilon}{\partial r^2} + \frac{\partial^2 v_r^\epsilon}{\partial z^2} + \frac{1}{r} \frac{\partial v_r^\epsilon}{\partial r} - \frac{v_r^\epsilon}{r^2} \right) + \frac{\partial p^\epsilon}{\partial r} = 0 \tag{3}$$

$$\rho \left( \frac{\partial v_z^\epsilon}{\partial t} + v_r^\epsilon \frac{\partial v_z^\epsilon}{\partial r} + v_z^\epsilon \frac{\partial v_z^\epsilon}{\partial z} \right) - \mu \left( \frac{\partial^2 v_z^\epsilon}{\partial r^2} + \frac{\partial^2 v_z^\epsilon}{\partial z^2} + \frac{1}{r} \frac{\partial v_z^\epsilon}{\partial r} \right) + \frac{\partial p^\epsilon}{\partial z} = 0 \tag{4}$$

$$\frac{\partial v_r^\epsilon}{\partial r} + \frac{\partial v_z^\epsilon}{\partial z} + \frac{v_r^\epsilon}{r} = 0 \tag{5}$$

Here  $\mathbf{v}^\epsilon = (v_r^\epsilon, v_z^\epsilon)$  is the fluid velocity,  $p^\epsilon$  is the pressure,  $\mu$  is fluid dynamic viscosity coefficient and  $\rho$  is fluid density.

The coupling between the fluid and the structure is obtained through the kinematic condition requiring continuity of the velocity evaluated at the deformed interface  $\Sigma_\epsilon(t)$

$$u_r^\epsilon(R + \eta^\epsilon(z, t), z, t) = \frac{\partial \eta^\epsilon(z, t)}{\partial t}, \quad u_z^\epsilon(R + \eta^\epsilon(z, t), z, t) = 0 \tag{6}$$

and the dynamic condition requiring continuity of contact forces at the deformed interface. Since the fluid contact force  $[(p^\epsilon - p_{\text{ref}})\mathbf{I} - 2\mu D(\mathbf{v}^\epsilon)]\mathbf{n} \cdot \mathbf{e}_r$  is given in Eulerian coordinates, where  $p_{\text{ref}}$  is the reference pressure, and the structure contact force (1) or (2) is given in Lagrangian coordinates, we must take into account the Jacobian of the transformation from Eulerian to Lagrangian coordinates  $J := \sqrt{\det((\nabla\phi)^T \nabla\phi)} = \sqrt{(R + \eta^\epsilon)^2 (1 + (\partial_z \eta^\epsilon)^2)}$ , where  $\phi : (z, \theta) \mapsto (x, y, z)$  and its gradient  $\nabla\phi$  are defined by

$$\begin{aligned} x &= (R + \eta^\epsilon) \cos \theta, \\ y &= (R + \eta^\epsilon) \sin \theta, \\ z &= z, \end{aligned} \quad \nabla\phi = \begin{pmatrix} \frac{\partial x}{\partial z} & \frac{\partial x}{\partial \theta} \\ \frac{\partial y}{\partial z} & \frac{\partial y}{\partial \theta} \\ 1 & 0 \end{pmatrix} = \begin{pmatrix} \frac{\partial \eta^\epsilon}{\partial z} \cos \theta & -(R + \eta^\epsilon) \sin \theta \\ \frac{\partial \eta^\epsilon}{\partial z} \sin \theta & (R + \eta^\epsilon) \cos \theta \\ 1 & 0 \end{pmatrix}$$

The coupling is then performed by requiring that for every Borel subset  $B$  of the lateral boundary  $\Sigma_\varepsilon$ , the contact force exerted by the fluid to the structure equals, but is of opposite sign to the contact force exerted by the structure to the fluid, namely,

$$\int_B [(p^\varepsilon - p_{\text{ref}})\mathbf{I} - 2\mu D(\mathbf{v}^\varepsilon)] \mathbf{n} \cdot \mathbf{e}_r J \, d\theta \, dz = \int_B f_r R \, d\theta \, dz$$

and so, pointwise, the dynamic coupling condition reads

$$[(p^\varepsilon - p_{\text{ref}})\mathbf{I} - 2\mu D(\mathbf{v}^\varepsilon)] \mathbf{n} \cdot \mathbf{e}_r \left(1 + \frac{\eta^\varepsilon}{R}\right) \sqrt{1 + (\partial_z \eta^\varepsilon)^2} = f_r \quad \text{on } \Sigma_\varepsilon \times \mathbb{R}^+ \quad (7)$$

where  $f_r$  is given by either (1) or (2).

Initially, the cylinder filled with fluid is assumed to be in an equilibrium. The reference configuration is that of  $\Sigma_\varepsilon$ , with the initial reference pressure  $p_{\text{ref}}$ . The initial conditions read:

$$\eta^\varepsilon = \frac{\partial \eta^\varepsilon}{\partial t} = 0 \quad \text{and} \quad \mathbf{v}^\varepsilon = 0 \quad \text{on } \Sigma_\varepsilon \times \{0\} \quad (8)$$

In this manuscript we assume that the flow is driven by the time-dependent dynamic pressure prescribed at both ends of the cylinder with the following inlet/outlet boundary conditions:

$$v_r^\varepsilon = 0, \quad p^\varepsilon + \rho(v_z^\varepsilon)^2/2 = P_0(t) + p_{\text{ref}} \quad \text{on } B_0^\varepsilon(t) \quad (9)$$

$$v_r^\varepsilon = 0, \quad p^\varepsilon + \rho(v_z^\varepsilon)^2/2 = P_L(t) + p_{\text{ref}} \quad \text{on } B_L^\varepsilon(t) \quad (10)$$

$$\eta^\varepsilon = 0 \quad \text{for } z = 0, \quad \eta^\varepsilon = 0 \quad \text{for } z = L \quad \text{and } \forall t \in \mathbb{R}_+ \quad (11)$$

assuming pressure drop to be  $A(t) = P_L(t) - P_0(t) \in C_0^\infty(0, +\infty)$ . This, of course, is not the only set of initial and boundary data that will give rise to a well-posed problem, see [20] for a discussion. We consider the current inlet/outlet boundary data primarily because we found these conditions to be reasonable and practical to work with. More precisely, we will see in Section 4.2 that in the reduced model, an  $\varepsilon^2$ -approximation of the inlet/outlet data requires only the inlet and outlet pressure to be prescribed, and this is something we can measure both in vitro and in vivo. Moreover, in [21] we showed that in the three-dimensional model with the inlet/outlet data requiring  $\eta^\varepsilon = 0$  and prescribed time-dependent dynamic pressure, a boundary layer forms to accommodate the transition from the zero displacement to the displacement dictated by the dynamic pressure condition. We proved in [21,27] that the contamination of the flow by the boundary layer decays exponentially fast away from the inlet/outlet boundaries. Therefore, except for a small neighborhood of the inlet/outlet boundary, the displacement will follow the dynamics determined by the time-dependent dynamic pressure.

Our goal is to derive the reduces equations approximating the original three-dimensional problem to the  $\varepsilon^2$  accuracy. To do that we write the problem in non-dimensional form and use asymptotic expansions for the velocity, displacement and pressure plugged into the equations to conclude which effects are negligible. An important component in this approach is to estimate the leading order behavior of the unknown functions by using a priori solution estimates. They will also provide an estimate for the flow regime that corresponds to the parameters in the problem, shown in Table 1.

### 3. The energy and a priori estimates

We start by the derivation of an energy estimate. To simplify notation introduce

$$C = \frac{hE}{1 - \sigma^2} \frac{1}{R^2} \left(1 + Q_{\text{ref}} + \frac{\beta^2}{12}\right), \quad Q_{\text{ref}} = \frac{p_{\text{ref}} R}{E} (1 - \sigma^2), \quad \beta = \begin{cases} 0, & \text{linear membrane} \\ \frac{h}{R}, & \text{linear Koiter} \end{cases} \quad (12)$$

Multiply the momentum equations by the velocity test function, integrate by parts and take into account the boundary conditions and the coupling at the lateral boundary to obtain

**Lemma 3.1.** *Solution  $\{\mathbf{v}^\varepsilon, \eta^\varepsilon\}$  satisfies the following energy equality*

$$\begin{aligned}
 & \frac{\rho}{2} \frac{d}{dt} \int_{\Omega_\varepsilon(t)} (\mathbf{v}^\varepsilon)^2 dV + 2\mu \int_{\Omega_\varepsilon(t)} D(\mathbf{v}^\varepsilon) \cdot D(\mathbf{v}^\varepsilon) dV + \frac{h\rho_S}{2} \frac{d}{dt} \int_0^L (\partial_t \eta^\varepsilon)^2 \pi R dz \\
 & + \frac{hE}{1-\sigma^2} \frac{d}{dt} \int_0^L \left( \frac{R^2 \beta^2}{12} (\partial_z^2 \eta^\varepsilon)^2 + \frac{\sigma}{6} \beta^2 (\partial_z \eta^\varepsilon)^2 + \frac{1}{R^2} \left( 1 + Q_{\text{ref}} + \frac{\beta^2}{12} \right) (\eta^\varepsilon)^2 \right) \pi R dz \\
 & = \int_{B_0^\varepsilon(t)} v_z^\varepsilon P_0(t) dS - \int_{B_L^\varepsilon(t)} v_z^\varepsilon P_L(t) dS
 \end{aligned} \tag{13}$$

Introduce the non-dimensional time  $\tilde{t} := \omega t$ , where  $\omega$  is the characteristic frequency, specified later in (19). From now on we will be working with the non-dimensional time  $\tilde{t}$  but will drop the ‘tilde’ notation for simplicity. The physical time  $t$  will be used later only in the final form of the reduced equations.

To get to the energy estimates we integrate the energy equality (13) with respect to time and take into account the rescaled time to get

$$\begin{aligned}
 & \frac{\rho\omega}{2} \|\mathbf{v}^\varepsilon\|^2 + 2\mu \int_0^t \|D(\mathbf{v}^\varepsilon)\|^2 + \rho_S \omega^3 \pi h R \|\partial_t \eta^\varepsilon\|^2 \\
 & + \pi \omega R \frac{hE}{1-\sigma^2} \int_0^t \left( \frac{1}{R^2} \left( 1 + Q_{\text{ref}} + \frac{\beta^2}{12} \right) (\eta^\varepsilon)^2 + \frac{\sigma}{6} \beta^2 (\partial_z \eta^\varepsilon)^2 + \frac{\beta^2 R^2}{12} (\partial_z^2 \eta^\varepsilon)^2 \right) dz \\
 & = \int_0^t \left\{ \int_{B_0(\tau)} v_z^\varepsilon P_0(\tau) dS - \int_{B_L(\tau)} v_z^\varepsilon P_L(\tau) dS \right\} d\tau
 \end{aligned} \tag{14}$$

We rewrite the expression under the time integral on the right-hand side as

$$\int_{\Omega_\varepsilon(\tau)} \text{div}(\hat{p} \mathbf{v}^\varepsilon) d\mathbf{x} - \int_{\Sigma(\tau)} \hat{p} \mathbf{v}^\varepsilon \cdot \mathbf{n} d\Sigma(\tau) = \int_{\Omega_\varepsilon(\tau)} \frac{A(\tau)}{L} v_z^\varepsilon d\mathbf{x} - \int_0^L \int_0^{2\pi} \hat{p} \omega \partial_\tau \eta^\varepsilon n_r J d\theta dz \tag{15}$$

where  $n_r = (R + \eta^\varepsilon) / \sqrt{(R + \eta^\varepsilon)^2 + (\partial_z \eta^\varepsilon)^2}$ ,  $J = \sqrt{(R + \eta^\varepsilon)^2 + (\partial_z \eta^\varepsilon)^2}$  and

$$\hat{p}(t) = \frac{A(t)}{L} z + P_0(t) \quad \text{where } A(t) = P_L(t) - P_0(t)$$

Then using (14) and (15) we get the following energy inequality

$$\begin{aligned}
 & \frac{\rho\omega}{2} \|\mathbf{v}^\varepsilon\|^2 + 2\mu \int_0^t \|D(\mathbf{v}^\varepsilon)\|^2 + \rho_S \omega^3 \pi h R \|\partial_t \eta^\varepsilon\|^2 + \pi \omega R C \int_0^L (\eta^\varepsilon)^2 dz \\
 & \leq \left| \int_0^t \left\{ \int_{\Omega_\varepsilon(\tau)} \frac{A(\tau)}{L} v_z^\varepsilon d\mathbf{x} - 2\pi \omega \int_0^L \hat{p} \partial_t \eta^\varepsilon (R + \eta^\varepsilon) dz \right\} d\tau \right|
 \end{aligned} \tag{16}$$

Estimate the right-hand side further in terms of the quantities on the left-hand side and the data.

**Proposition 3.2.** *For any  $\alpha > 0$  the following holds*

$$\left| \int_0^t \int_{\Omega_\varepsilon(\tau)} \frac{A(\tau)}{L} v_z^\varepsilon d\mathbf{x} d\tau \right| \leq \frac{\rho\alpha\omega}{2} \int_0^t \|v_z^\varepsilon\|_{L^2(\Omega_\varepsilon(\tau))}^2 d\tau + \frac{\pi R^2}{\rho\alpha\omega L} \int_0^t |A(\tau)|^2 d\tau + \frac{\pi \|\hat{p}\|_\infty^2}{\rho_S \alpha \omega h R} \int_0^t \|\eta^\varepsilon\|_{L^2}^2 d\tau$$

Similarly, the second term on the right-hand side can be estimated as follows:

**Proposition 3.3.** For any  $\alpha > 0$  the following holds

$$\begin{aligned} \left| 2\pi\omega \int_0^t \int_0^L \hat{p} \partial_t \eta^\varepsilon (R + \eta^\varepsilon) dz d\tau \right| &\leq \pi\omega\alpha RC \int_0^t \|\eta^\varepsilon\|_{L^2}^2 + \pi\omega \frac{\|\hat{p}\|_\infty^2}{\alpha C} \int_0^t \|\partial_t \eta^\varepsilon\|_{L^2}^2 \\ &+ \frac{8\pi R\omega}{C} \int_0^L |\hat{p}|^2 dz + \frac{8\pi\omega LR}{C} \left( \sup_z \int_0^t |\partial_t \hat{p}| d\tau \right)^2 + \frac{\pi\omega RC}{8} \|\eta^\varepsilon\|_{L^2}^2 + \frac{\pi\omega RC}{8} \sup_t \|\eta^\varepsilon\|^2 \end{aligned}$$

Use these results to estimate the right-hand side of (16) and take the supremum over time of the right-hand side to get

$$\begin{aligned} &\frac{\rho\omega}{2} \|\mathbf{v}^\varepsilon\|_{L^2(\Omega_\varepsilon(t))}^2 + \pi\omega^3 \rho_S h R \|\partial_t \eta^\varepsilon\|^2 + \pi\omega RC \|\eta^\varepsilon\|^2 \\ &\leq \frac{\rho\alpha\omega}{2} \int_0^t \|\mathbf{v}_z^\varepsilon\|_{L^2(\Omega_\varepsilon(\tau))}^2 d\tau + \left( \pi\omega\alpha RC + \frac{\pi\|\hat{p}\|_\infty^2}{\rho_S\alpha\omega h R} \right) \int_0^t \|\eta^\varepsilon\|_{L^2}^2 d\tau + \pi\omega \frac{\|\hat{p}\|_\infty^2}{\alpha RC} \int_0^t \|\partial_t \eta^\varepsilon\|^2 d\tau \\ &+ \frac{8\pi R\omega}{C} \int_0^L \hat{p}^2 dz + \frac{8\pi\omega LR}{C} \left( \sup_z \int_0^t |\partial_t \hat{p}| d\tau \right)^2 + \frac{\pi R^2}{\rho\alpha\omega L} \int_0^t |A(\tau)|^2 d\tau + \frac{\pi\omega RC}{4} \sup_t \|\eta^\varepsilon\|_{L^2}^2 \end{aligned}$$

Define

$$y(t) = \int_0^t \left\{ \frac{\rho\omega}{2} \|\mathbf{v}^\varepsilon\|_{L^2(\Omega_\varepsilon(\tau))}^2 + \pi\omega^3 \rho_S h R \|\partial_t \eta^\varepsilon\|^2 + \pi\omega RC \|\eta^\varepsilon\|^2 \right\} d\tau \quad (17)$$

Then we have

$$\begin{aligned} y'(t) &\leq \left( \alpha + \frac{\|\hat{p}\|_\infty^2}{\alpha\rho_S\omega^2 h R^2 C} \right) y(t) + \frac{\pi\omega RC}{4} \sup_t \|\eta^\varepsilon\|^2 + \frac{8\pi R\omega}{C} \int_0^L \hat{p}^2 dz \\ &+ \frac{8\pi\omega LR}{C} \left( \sup_z \int_0^t |\partial_t \hat{p}| d\tau \right)^2 + \frac{\pi R^2}{\rho\alpha\omega L} \int_0^t |A(\tau)|^2 d\tau \end{aligned}$$

Now take  $\alpha$  so that  $\|\hat{p}\|_\infty^2 / (\alpha\rho_S\omega^2 h R^2 C) \leq \alpha$  and let  $t_0$  be such that  $\max_{[0,T]} y'(t) = y'(t_0)$ . Then  $|y(t)| \leq T|y'(t_0)|$ , and so we get

$$\begin{aligned} y'(t_0) &\leq 2\alpha T y'(t_0) + \frac{\pi\omega RC}{4} \sup_t \|\eta^\varepsilon\|^2 + \frac{8\pi R\omega}{C} \int_0^L \hat{p}^2 dz + \frac{8\pi\omega LR}{C} \left( \sup_z \int_0^t |\partial_t \hat{p}| d\tau \right)^2 \\ &+ \frac{\pi R^2}{\rho\alpha\omega L} \int_0^t |A(\tau)|^2 d\tau \end{aligned}$$

Choose, for example,  $\alpha = \frac{1}{4T}$ . Then

$$\frac{1}{2} y'(t_0) \leq \frac{\pi\omega RC}{4} \sup_t \|\eta^\varepsilon\|^2 + \frac{8\pi R\omega}{C} \int_0^L \hat{p}^2 dz + \frac{8\pi\omega LR}{C} \left( \sup_z \int_0^t |\partial_t \hat{p}| d\tau \right)^2 + \frac{4T\pi R^2}{\rho\omega L} \int_0^t |A(\tau)|^2 d\tau$$

Take into account the definition of  $y$ , given by (17), and combine the terms containing the  $L^2$ -norm of  $\eta^\varepsilon$  on both sides to get

$$\begin{aligned} & \frac{\rho\omega}{2} \|v^\varepsilon\|_{L^2(\Omega_\varepsilon(t))}^2 + \pi\omega^3 \rho_S h R \|\partial_t \eta^\varepsilon\|^2 + \frac{\pi\omega RC}{2} \|\eta^\varepsilon\|^2 \\ & \leq \frac{16\pi LR\omega}{C} \left( \sup_{z,t} |\hat{p}|^2 + \left( \sup_z \int_0^t |\partial_t \hat{p}| \, d\tau \right)^2 \right) + \frac{8T\pi R^2}{\rho\omega L} \int_0^t |A(\tau)|^2 \, d\tau \end{aligned} \tag{18}$$

We now choose the characteristic frequency  $\omega$  so that all the terms on the right-hand side contribute with the same weight. Namely, we set the coefficient in front of the pressure term  $\hat{p}$  and its time derivative equal to the coefficient in front of the pressure drop term  $A(\tau)$  to get

$$\omega = \frac{1}{L} \sqrt{\frac{RC}{2\rho}} = \frac{1}{L} \sqrt{\frac{hE(1 + Q_{\text{ref}} + \beta^2/12)}{2\rho R(1 - \sigma^2)}} \tag{19}$$

We remark that  $\omega L$  is exactly the structure “sound speed” derived by Fung in [11] for the linear membrane model. Finally, after dividing both sides of inequality (18) by  $\omega$  we get

**Theorem 3.4.** *The following energy inequality holds for the solution  $\{v^\varepsilon, \eta^\varepsilon\}$  of the coupled fluid–structure interaction problem described in Section 2*

$$\frac{\rho}{2} \|v^\varepsilon\|_{L^2(\Omega_\varepsilon(t))}^2 + \pi\omega^2 \rho_S h R \|\partial_t \eta^\varepsilon\|^2 + \frac{\pi R}{2} C \|\eta^\varepsilon\|^2 \leq \frac{16\pi LR}{C} \mathcal{P}^2$$

where  $\mathcal{P}^2 := \sup_{z,t} |\hat{p}|^2 + (\sup_z \int_0^t |\partial_t \hat{p}| \, d\tau)^2 + T \int_0^t |A(\tau)|^2$  and  $C$  is defined by (12).

From this results we get the following a priori solution estimates.

**Lemma 3.5.** *Solution  $\{v^\varepsilon, \eta^\varepsilon\}$  of the fluid–structure interaction problem satisfies the following a priori estimates*

$$\begin{aligned} & \frac{1}{L} \|\eta^\varepsilon(t)\|_{L^2(0,L)}^2 \leq \frac{32}{C^2} \mathcal{P}^2, \quad \frac{1}{L} \|\partial_t \eta^\varepsilon(t)\|_{L^2(0,L)}^2 \leq \frac{16}{\rho_S \omega^2 h C} \mathcal{P}, \quad \frac{1}{LR^2\pi} \|v^\varepsilon\|_{L^2(\Omega_\varepsilon(t))}^2 \leq \frac{32}{\rho RC} \mathcal{P}^2 \\ & \int_0^t \left\{ \|\partial_r v_r^\varepsilon\|_{L^2(\Omega_\varepsilon(\tau))}^2 + \left\| \frac{v_r^\varepsilon}{r} \right\|_{L^2(\Omega_\varepsilon(\tau))}^2 + \|\partial_z v_z^\varepsilon\|_{L^2(\Omega_\varepsilon(\tau))}^2 \right\} d\tau \leq \frac{4\pi R^2}{\mu} \sqrt{\frac{2}{\rho RC}} \mathcal{P}^2 \\ & \int_0^t \left\{ \|\partial_r v_z^\varepsilon\|_{L^2(\Omega_\varepsilon(\tau))}^2 + \|\partial_z v_r^\varepsilon\|_{L^2(\Omega_\varepsilon(\tau))}^2 \right\} d\tau \leq \frac{4R^2}{\mu} \sqrt{\frac{2}{\rho RC}} \mathcal{P}^2 \end{aligned}$$

where  $C$  is defined by (12).

**Corollary 3.6.** *For the Koiter shell model the following holds*

$$\frac{1}{L} \|\partial_z \eta^\varepsilon(t)\|_{L^2(0,L)}^2 \leq \frac{96}{\sigma h^2 C^2} \mathcal{P}^2, \quad \frac{1}{L} \|\partial_z^2 \eta^\varepsilon(t)\|_{L^2(0,L)}^2 \leq \frac{192}{R^2 h^2 C^2} \mathcal{P}^2, \quad \|\eta^\varepsilon(t)\|_{L^\infty(0,L)} \leq \frac{4L}{hC} \sqrt{\frac{6}{\sigma}} \mathcal{P}$$

where  $C$  is defined by (12).

Using the a priori estimates we obtain the asymptotic expansions and derive the reduced equations in the next section.

### 4. The effective equations

#### 4.1. Asymptotic expansions

First write the underlying equations in non-dimensional form. For that purpose introduce the following non-dimensional independent variables  $\tilde{r}$ ,  $\tilde{z}$  and  $\tilde{t}$

$$r = R\tilde{r}, \quad z = L\tilde{z}, \quad t = \frac{1}{\omega} \tilde{t}, \quad \text{where } \omega = \frac{1}{L} \sqrt{\frac{hE(1 + Q_{\text{ref}} + \beta^2/12)}{R\rho(1 - \sigma^2)}} \tag{20}$$

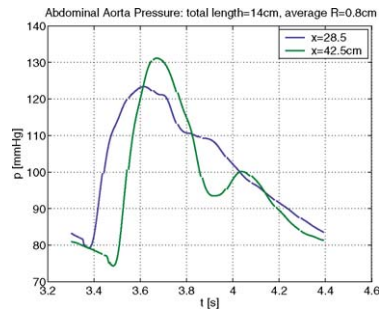


Fig. 2. Inlet/outlet aortic pressure.

Fig. 2. La pression artérielle à l'entrée/sortie [22].

Table 1

Table with parameter values

Tableau 1

Tableau contenant les valeurs des paramètres

Parameters	Aorta/Iliacs	Latex tube
Char. radius $R$ (m)	0.006–0.012 (0.008) [1]	0.011
Char. length $L$ (m)	0.065–0.2 (0.14)	0.34
Dyn. viscosity $\mu$ (kg/m s)	$3.5 \times 10^{-3}$	$3.5 \times 10^{-3}$
Young's modulus $E$ (Pa)	$10^5$ – $10^6$ ( $5 \times 10^5$ ) [2]	$1.0587 \times 10^6$
Wall thickness $h$ (m)	$1$ – $2 \times 10^{-3}$ [1]	0.0009
Wall density $\rho_S$ (kg/m <sup>2</sup> )	1.1 [1]	1.1
Fluid density $\rho$ (kg/m <sup>3</sup> )	1050	1000

Using the a priori estimates obtained in Section 3 we introduce the following asymptotic expansions

$$\mathbf{v}^\varepsilon = V \{ \tilde{\mathbf{v}}^0 + \varepsilon \tilde{\mathbf{v}}^1 + \dots \}, \quad \text{where } 2V = \sqrt{\frac{R(1-\sigma^2)}{\rho h E (1 + Q_{\text{ref}} + \beta^2/12)}} \mathcal{P} \quad (21)$$

$$\eta^\varepsilon = \Phi \{ \tilde{\eta}^0 + \varepsilon \tilde{\eta}^1 + \dots \}, \quad \text{where } 2\Phi = \frac{R^2(1-\sigma^2)}{h E (1 + Q_{\text{ref}} + \beta^2/12)} \mathcal{P}, \quad \text{and } p^\varepsilon = \rho V^2 \{ \tilde{p}^0 + \varepsilon \tilde{p}^1 + \dots \}. \quad (22)$$

Since the estimates obtained in the previous section present the upper bounds for the behavior of the unknown functions, in expansions (21), (22) we used the *scaled* upper bounds to only capture how the magnitude of the unknown functions changes with a given parameter. For example, we see that the magnitude of the vessel wall displacement increases as the square of the reference radius  $R$  and decreases with the increase of the vessel wall thickness  $h$  and Young's modulus  $E$ .

In this article we want to develop a reduced effective model that is a good approximation of the fluid–structure interaction problem for the parameter values and the pressure data corresponding to the abdominal aorta and iliac arteries, given in Table 1. Using these values (the values given in parentheses) we obtain  $V = 0.5$  m/s,  $\Phi = 2.5 \times 10^{-4}$  m,  $\omega = 113$ . These are in excellent agreement with the values measured in human abdominal aorta, see [2], for which the average velocity is around 0.5 m/s and radial displacement is below 10 percent of the reference radius. Notice that our value of  $\Phi$  is around 3 percent of the reference radius  $R = 0.008$  m.

Using a standard approach, presented in detail in [20], based on plugging expansions (21), (22) into Eqs. (1)–(5) and ignoring the terms of order  $\varepsilon^2$  and smaller, we obtain:

- The  $\varepsilon^2$ -approximation of the pressure is hydrostatic, namely,  $\tilde{p} = \tilde{p}^0 + \varepsilon \tilde{p}^1$  is constant across the cross-section of the tube,  $\partial \tilde{p} / \partial \tilde{r} = 0$ . This follows from the conservation of radial momentum equation.
- The following two-dimensional initial-boundary value problem defined on the scaled domain describes an  $\varepsilon^2$  approximation of the fluid–structure interaction problem



$$Sh \frac{\partial \tilde{v}_z}{\partial \tilde{t}} + \tilde{v}_z \frac{\partial \tilde{v}_z}{\partial \tilde{z}} + \tilde{v}_r \frac{\partial \tilde{v}_z}{\partial \tilde{r}} + \frac{\partial \tilde{p}}{\partial \tilde{z}} = \frac{1}{Re} \left\{ \frac{1}{\tilde{r}} \frac{\partial}{\partial \tilde{r}} \left( \tilde{r} \frac{\partial \tilde{v}_z}{\partial \tilde{r}} \right) \right\} \quad (23)$$

$$\frac{\partial}{\partial \tilde{r}} (\tilde{r} \tilde{v}_r) + \frac{\partial}{\partial \tilde{z}} (\tilde{r} \tilde{v}_z) = 0 \quad (24)$$

Lateral boundary:  $\tilde{p} - \tilde{p}_{\text{ref}} = \frac{\mathcal{P}}{\rho V^2} \tilde{\eta}, \quad (\tilde{v}_r, \tilde{v}_z) = \left( \frac{\partial \tilde{\eta}}{\partial \tilde{t}}, 0 \right) \quad (25)$

Inlet/Outlet:  $\tilde{\eta} = 0, \tilde{v}_{\tilde{r}} = 0 \quad \text{and} \quad \tilde{p} = (P_{0/L}(\tilde{t}) + p_{\text{ref}})/(\rho V^2) \quad (26)$

Initial data:  $\tilde{\eta} = \frac{\partial \tilde{\eta}}{\partial \tilde{t}} = 0 \quad (27)$

where  $\tilde{v}_r := \tilde{v}_r^1 + \varepsilon \tilde{v}_r^2$  so that  $v_r^\varepsilon = \varepsilon V(\tilde{v}_r + \mathcal{O}(\varepsilon^2))$ ,  $\tilde{v}_z := \tilde{v}_z^0 + \varepsilon \tilde{v}_z^1$  so that  $v_z^\varepsilon = V(\tilde{v}_z + \mathcal{O}(\varepsilon^2))$ ,  $\tilde{p} := \tilde{p}^0 + \varepsilon \tilde{p}^1$  so that  $p^\varepsilon = \rho V^2(\tilde{p} + \mathcal{O}(\varepsilon^2))$  and  $\tilde{\eta} := \tilde{\eta}^0 + \varepsilon \tilde{\eta}^1$  so that  $\eta^\varepsilon = \Phi(\tilde{\eta} + \mathcal{O}(\varepsilon^2))$ . Here the Strouhal and the Reynolds numbers are given by

$$Sh = \frac{L\omega}{V} \quad \text{and} \quad Re = \frac{\rho V R^2}{\mu L} \quad (28)$$

For the parameter values from Table 1 we get  $Sh = 31$  and  $Re = 69$ . Notice that Eq. (25) says that the leading-order term that survives from the fluid contact force is the pressure term, and that the  $\varepsilon^2$ -approximation of the contact force corresponding to the linear Koiter shell model consists of only the displacement term shown in (25). The derivative terms turn out to be all of higher order. Furthermore, notice the  $\varepsilon^2$ -approximation of the inlet and outlet boundary conditions consists of prescribing only the pressure and not the dynamic pressure.

#### 4.2. The reduced equations

Although problem (23)–(27) presents a simplification of the three-dimensional fluid–structure interaction problem described in Section 2, it is still rather involving and difficult to study this problem both theoretically and numerically. This is why further simplifications have been obtained in the literature. They are based on averaging equations (23), (24) with respect to the cross-sectional area leading to a system of one-dimensional equations of hyperbolic type. These equations have two major drawbacks: (i) They are not closed (ad hoc assumptions on the axial velocity profile needs to be used to obtain a closed system); (ii) Due to their hyperbolic nature, prescribing the pressure at the inlet and at the outlet gives rise to the reflected waves that are not physiologically reasonable. In the present article we obtain an effective model that gets around both drawbacks. We obtain a *closed* system of reduced equations that is of mixed hyperbolic-parabolic type, displaying explicitly the physiologically observed *viscoelastic* nature of the coupled problem, see Eqs. (39) and (41). Furthermore, the mixed system ‘allows’ prescribing the inlet and outlet pressures without exhibiting reflections appearing in the one-dimensional hyperbolic problems, see Section 5.

To derive the reduced effective equations that approximate the original three-dimensional problem to the  $\varepsilon^2$  accuracy we rely on the ideas presented by the authors in [20] utilizing homogenization theory in porous media flows. Once the proper motivation is established the calculation of the effective equations itself can be performed using formal asymptotic theory, which we now utilize.

Consider Eq. (23) and the values of the non-dimensional parameters  $Sh = 31$  and  $Re = 69$ . Multiply Eq. (23) by  $\varepsilon$  and define the rescaled non-dimensional parameters

$$Sh_0 = \varepsilon Sh = \frac{R\omega}{V}, \quad Re_0 = \frac{Re}{\varepsilon} = \frac{\rho R V}{\mu} \quad (29)$$

Notice that now the Reynolds number  $Re_0$  is the ‘usual’ local Reynolds number, reading  $Re = 1200$ , and that  $Sh_0$  is of order one,  $Sh_0 = 1.8$ . Introduce the rescaled pressure

$$p = \frac{\rho L V^2}{R} \tilde{\tilde{p}} = \rho V^2 \frac{1}{\varepsilon} \tilde{\tilde{p}} = \rho V^2 \tilde{p}, \quad \text{so} \quad \tilde{\tilde{p}} = \varepsilon \tilde{p} \quad (30)$$

and notice that the nonlinear advection terms are now of order  $\varepsilon$ . Look for a solution which is in the form of the leading, zero-th order approximation plus its  $\varepsilon$  correction. The nonlinear terms will not appear in the leading order

approximation, but only in the calculation of the  $\varepsilon$  correction. Proceed by rescaling the pressure in the leading-order momentum equation resulting from (23) and average across the cross-section of the leading-order mass equation corresponding to (24). One gets the following system for the *zero-th order approximation* of the solution, written in dimensional variables, defined on the domain  $0 \leq z \leq L, 0 \leq r \leq R + \eta^0(z, t)$ :

$$\frac{\partial(R + \eta^0)^2}{\partial t} + \frac{\partial}{\partial z} \int_0^{R+\eta^0} 2rv_z^0 dr = 0 \tag{31}$$

$$\rho \frac{\partial v_z^0}{\partial t} + \frac{\partial}{\partial z} \left( \frac{hE(1 + Q_{\text{ref}} + \beta^2/12)}{R(1 - \sigma^2)} \frac{\eta^0}{R + \eta^0} \right) = \mu \frac{1}{r} \frac{\partial}{\partial r} \left( r \frac{\partial v_z^0}{\partial r} \right) \tag{32}$$

$$v_z^0(0, z, t) \text{ bounded, } v_z^0(R + \eta^0(z, t), z, t) = 0 \text{ and } v_z^0(r, z, 0) = 0 \tag{33}$$

$$p = P_{0/L}(t) + p_{\text{ref}} \text{ for } z = 0/L, 0 \leq r \leq R \text{ and } \forall t \in \mathbb{R}_+ \tag{34}$$

The pressure  $p$  is linked to  $\eta^0$  via

$$p(z, t) = p_{\text{ref}} + \frac{hE(1 + Q_{\text{ref}} + \beta^2/12)}{R(1 - \sigma^2)} \frac{\eta^0}{R} \tag{35}$$

The system for the  $\varepsilon$ -correction of the solution is obtained by first noticing that the  $\varepsilon$ -order conservation of mass equation (24), integrated, implies an explicit formula for  $\tilde{v}_r^1$ :

$$rv_r^1(r, z, t) = (R + \eta^0) \frac{\partial \eta^0}{\partial t} + \int_r^{R+\eta^0} \frac{\partial v_z^0}{\partial z}(\xi, z, t) \xi d\xi \tag{36}$$

Next we focus on the  $\varepsilon$ -order equations derived from (23) and linearize the nonlinear advection term around the zero-order approximation. We obtain an equation that is not closed due to the presence of the term  $\partial \tilde{p}^1 / \partial \tilde{z}$ . However, since  $\tilde{p}^1$  is zero at the lateral boundary  $\tilde{r} = 1 + \Phi/R\tilde{\eta}^0$ , and since  $\tilde{p}^1$  is independent of  $\tilde{r}$ , we conclude that  $\tilde{p}^1 = 0$ . Thus, we obtain the following closed problem for the  $\varepsilon$  correction of the velocity, defined on the domain  $0 \leq z \leq L, 0 \leq r \leq R + \eta^0(z, t)$  written in dimensional form

$$\frac{\partial v_z^1}{\partial t} - v \frac{1}{r} \frac{\partial}{\partial r} \left( r \frac{\partial v_z^1}{\partial r} \right) = -S_{v_z^1}(r, z, t) \tag{37}$$

$$v_z^1(0, z, t) \text{ bounded, } v_z^1(R + \eta^0(z, t), z, t) = 0, \quad v_z^1(r, 0, t) = v_z^1(r, L, t) = 0 \text{ and } v_z^1(r, z, 0) = 0 \tag{38}$$

where  $S_{v_z^1}(r, z, t) = v_r^1 \partial v_z^0 / \partial r + v_z^0 \partial v_z^0 / \partial z$  is the linearized advection term containing the already calculated function. Here  $v = \mu/\rho$  is the kinematic viscosity coefficient. Notice that the boundary condition is evaluated at the deformed boundary whose  $\varepsilon^2$ -approximation is obtained in the previous step.

**Theorem 4.1.** *The velocity field  $(\tilde{v}_z^0 + \varepsilon \tilde{v}_z^1, \varepsilon \tilde{v}_r^1)$  and the pressure field  $\frac{1}{\varepsilon} \tilde{p}^0$  satisfy Eqs. (23)–(27) to  $\mathcal{O}(\varepsilon^2)$ .*

The proof is the same as that of Proposition 7.1 in [20].

### 4.3. In summary

Functions  $\{(v_z^0 + v_z^1, v_r^1), \eta^0, p\}$ , where  $v_z^0, \eta^0, p$  satisfy problem (31)–(35),  $v_r^1$  solves (36) and  $v_z^1$  solves (37), (38), satisfy the fluid–structure interaction problem described in Section 2 to the  $\varepsilon^2$ -accuracy. The reduced equations hold under the following assumptions:

- (i) The domain is axially symmetric with small aspect ratio  $\varepsilon = R/L \ll 1$ ;
- (ii) Longitudinal displacement is negligible;
- (iii) Radial displacement is not too large, i.e.,  $\Phi/R \leq \varepsilon$ ;
- (iv) The initial tube radius is constant;

- (v) The  $Sh$  number is not small, i.e.,  $Sh > 1$ , and  $Re$  is medium;
- (vi) The  $z$ -derivatives of the non-dimensional quantities are of order  $O(1)$ .

4.4. Expansion with respect to the radial displacement

We simplify our problem further by introducing the expansions with respect to the small parameter  $\delta := \Phi/R$ . This parameter measures the size of the radial displacement in non-dimensional variables:

$$\begin{aligned} \tilde{\eta}^0 &= \tilde{\eta}^{0,0} + \delta \tilde{\eta}^{0,1} + \dots, & \tilde{p}^0 &= \tilde{p}^{0,0} + \delta \tilde{p}^{0,1} + \dots, \\ \tilde{v}_z^0 &= \tilde{v}_z^{0,0} + \delta \tilde{v}_z^{0,1} + \dots, & \tilde{v}_z^1 &= \tilde{v}_z^{1,0} + \dots, & \tilde{v}_r^1 &= \tilde{v}_r^{1,0} + \dots \end{aligned}$$

In dimensional variables we have

$$\begin{aligned} \eta &= \eta^{0,0} + \eta^{0,1} + \dots = \Phi(\tilde{\eta}^{0,0} + \delta \tilde{\eta}^{0,1} + \dots), & \text{where } \eta^{0,0} &= \Phi \tilde{\eta}^{0,0}, \eta^{0,1} = \Phi \delta \tilde{\eta}^{0,1} \\ v_z &= v_z^{0,0} + v_z^{0,1} + v_z^{1,0} + \dots = V(\tilde{v}_z^{0,0} + \delta \tilde{v}_z^{0,1} + \varepsilon \tilde{v}_z^{1,0} + \dots) & v_r &= v_r^{1,0} + \dots = V(\varepsilon \tilde{v}_r^{1,0} + \dots). \end{aligned}$$

Following a similar approach as in [20] one obtains that Eqs. (31)–(35) and (36)–(38) imply the following leading-order problems, written in dimensional form.

4.4.1. The zero-th order approximation

Find  $v_z^{0,0}(r, z, t)$ ,  $\eta^{0,0}(z, t)$  and  $p^{0,0}(z, t)$  such that

$$\begin{cases} \frac{\partial \eta^{0,0}}{\partial t} + \frac{1}{R} \frac{\partial}{\partial z} \int_0^R r v_z^{0,0} dr = 0 \\ \rho \frac{\partial v_z^{0,0}}{\partial t} - \mu \frac{1}{r} \frac{\partial}{\partial r} \left( r \frac{\partial v_z^{0,0}}{\partial r} \right) = -\frac{\partial p^{0,0}}{\partial z}(z, t), & \frac{\partial p^{0,0}}{\partial z}(z, t) = \frac{Eh(1 + Q_{ref} + \beta^2/12)}{R^2(1 - \sigma^2)} \frac{\partial \eta^{0,0}}{\partial z} \end{cases} \tag{39}$$

$$\begin{cases} v_z^{0,0}(0, z, t) \text{ bounded, } v_z^{0,0}(R, z, t) = 0, & p^{0,0}(z, 0) = p_{ref}, \quad \eta^{0,0}(z, 0) = v_z^{0,0}(r, z, 0) = 0 \\ \eta^{0,0}(0, t) = P_0(t)/C, & \eta^{0,0}(L, t) = P_L(t)/C \end{cases} \tag{40}$$

Then recover the  $\delta = \Phi/R$ -correction  $v_z^{0,1}(r, z, t)$ ,  $\eta^{0,1}(z, t)$  and  $p^{0,1}(z, t)$  by solving

$$\begin{cases} \frac{\partial \eta^{0,1}}{\partial t} + \frac{1}{R} \frac{\partial}{\partial z} \int_0^R r v_z^{0,1} dr = -\frac{1}{R} \eta^{0,0} \frac{\partial \eta^{0,0}}{\partial t} \\ \rho \frac{\partial v_z^{0,1}}{\partial t} - \mu \frac{1}{r} \frac{\partial}{\partial r} \left( r \frac{\partial v_z^{0,1}}{\partial r} \right) = -\frac{\partial p^{0,1}}{\partial z}(z, t), & \frac{\partial p^{0,1}}{\partial z}(z, t) = \frac{Eh(1 + Q_{ref} + \beta^2/12)}{R^2(1 - \sigma^2)} \frac{\partial \eta^{0,1}}{\partial z} \end{cases} \tag{41}$$

$$\begin{cases} v_z^{0,1}(0, z, t) \text{ bounded, } v_z^{0,1}(R, z, t) = -\eta^{0,0} \frac{\partial v_z^{0,0}}{\partial r}(R, z, t) \\ p^{0,1}(z, 0) = 0, & \eta^{0,1}(z, 0) = v_z^{0,1}(r, z, 0) = 0, \quad \eta^{0,1}(0, t) = \eta^{0,1}(L, t) = 0 \end{cases} \tag{42}$$

Before we state the  $\epsilon$ -correction observe that (39)–(42) can be solved efficiently by considering

$$\begin{cases} \frac{\partial \zeta}{\partial t} - \frac{1}{r} \frac{\partial}{\partial r} \left( r \frac{\partial \zeta}{\partial r} \right) = 0 & \text{in } (0, R) \times (0, \infty) \\ \zeta(0, t) \text{ is bounded, } & \zeta(R, t) = 0 \quad \text{and} \quad \zeta(r, 0) = 1 \end{cases} \tag{43}$$

and the mean of  $\zeta$  in the radial direction  $\mathcal{K}(t) = 2 \int_0^R \zeta(r, t) r dr$ , which can both be evaluated in terms of the Bessel’s functions. Our solution can then be written in terms of the following operators

$$(\zeta \star f)(r, z, t) := \int_0^t \zeta \left( r, \frac{\mu(t - \tau)}{\rho} \right) f(z, \tau) d\tau, \quad (\mathcal{K} \star f)(z, t) := \int_0^t \mathcal{K} \left( \frac{\mu(t - \tau)}{\rho} \right) f(z, \tau) d\tau$$

This approach will uncover the visco-elastic nature of the coupled fluid–structure interaction problem since the resulting equations will have the form of a Biot system with memory. Namely, the problem now consists of finding  $\eta^{0,0}$ ,  $p^{0,0}$ ,  $v_z^{0,0}$  by solving the following initial-boundary value problem of Biot type with memory:

$$\begin{cases} \frac{\partial \eta^{0,0}}{\partial t}(z, t) = \frac{C}{2\rho R} \frac{\partial^2 (\mathcal{K} \star \eta^{0,0})}{\partial z^2}(z, t) & \text{on } (0, L) \times (0, +\infty) \\ \eta^{0,0}(0, t) = P_0(t)/C, \quad \eta^{0,0}(L, t) = P_L(t)/C & \text{and } \tilde{\eta}^{0,0}(z, 0) = 0 \end{cases} \quad (44)$$

Recover  $\frac{\partial p^{0,0}}{\partial z}(z, t) = C \frac{\partial \eta^{0,0}}{\partial z}(z, t)$ . Calculate  $v_z^{0,0}$  by solving

$$\begin{cases} \rho \frac{\partial v_z^{0,0}}{\partial t} - \mu \frac{1}{r} \frac{\partial}{\partial r} \left( r \frac{\partial v_z^{0,0}}{\partial r} \right) = -\frac{\partial p^{0,0}}{\partial z}(z, t) \\ v_z^{0,0}(0, z, t) \text{ bounded, } v_z^{0,0}(R, z, t) = 0 \end{cases} \quad (45)$$

Recover the  $\delta$ -correction  $\eta^{0,1}$ ,  $p^{0,1}$ ,  $v_z^{0,1}$  by solving the following initial-boundary value problem:

$$\begin{cases} \frac{\partial \eta^{0,1}}{\partial t}(z, t) = \frac{C}{2\rho R} \frac{\partial^2 (\mathcal{K} \star \eta^{0,1})}{\partial z^2}(z, t) - S_{\eta^{0,1}}(z, t) \\ \eta^{0,1}(0, t) = \eta^{0,1}(L, t) = 0 & \text{and } \eta^{0,1}(z, 0) = 0 \end{cases} \quad (46)$$

where

$$S_{\eta^{0,1}}(z, t) := \frac{1}{R} \eta^{0,0} \frac{\partial \eta^{0,0}}{\partial t} - \frac{R}{2} \frac{\partial}{\partial z} \left( \eta^{0,0} \frac{\partial v_z^{0,0}}{\partial r} \Big|_{r=R} \right) + \frac{1}{2R} \frac{\partial}{\partial z} \left( \mathcal{K} \star \frac{\partial}{\partial t} \left( \eta^{0,0} \frac{\partial v_z^{0,0}}{\partial r} \Big|_{r=R} \right) \right)$$

Recover  $\frac{\partial p^{0,1}}{\partial z}(z, t) = C \frac{\partial \eta^{0,1}}{\partial z}(z, t)$ . Calculate  $v_z^{0,1}$  by solving

$$\begin{cases} \rho \frac{\partial v_z^{0,1}}{\partial t} - \mu \frac{1}{r} \frac{\partial}{\partial r} \left( r \frac{\partial v_z^{0,1}}{\partial r} \right) = -\frac{\partial p^{0,1}}{\partial z}(z, t) \\ v_z^{0,1}(0, z, t) \text{ bounded, } v_z^{0,1}(R, z, t) = -\eta^{0,0} \frac{\partial v_z^{0,0}}{\partial r}(R, z, t) \end{cases} \quad (47)$$

#### 4.4.2. The $\varepsilon$ -correction

Solve for  $v_z^{1,0} = v_z^{1,0}(r, z, t)$  and  $v_r^{1,0} = v_r^{1,0}(r, z, t)$  by first recovering  $v_r^{1,0}$  via

$$r v_r^{1,0}(r, z, t) = R \frac{\partial \eta^{0,0}}{\partial t} + \int_0^R \frac{\partial v_z^{0,0}}{\partial z}(\xi, z, t) \xi \, d\xi \quad (48)$$

and then solve the following linear problem for  $v_z^{1,0}$  defined on  $(0, R) \times (0, L) \times (0, \infty)$

$$\begin{cases} \frac{\partial v_z^{1,0}}{\partial t} - v \frac{1}{r} \frac{\partial}{\partial r} \left( r \frac{\partial v_z^{1,0}}{\partial r} \right) = -S_{v_z^{1,0}}(r, z, t) \\ v_z^{1,0}(0, z, t) \text{ bounded, } v_z^{1,0}(R, z, t) = 0 \\ v_z^{1,0}(r, 0, t) = v_z^{1,0}(r, L, t) = 0 & \text{and } v_z^{1,0}(r, z, 0) = 0 \end{cases} \quad (49)$$

where  $S_{v_z^{1,0}}(r, z, t) = v_r^{1,0} \partial v_z^{0,0} / \partial r + v_z^{0,0} \partial v_z^{0,0} / \partial z$ .

Biot systems were first introduced by Biot in the 1950s [23] and derived formally from first principles in the case of porous media flows with linear elastic structure undergoing small vibrations in the seventies. We refer to [24] and [25] and the references therein for details. For a review of the mathematically rigorous homogenization results related to these models we refer to [26].

## 5. Numerical method

First rewrite the approximations in the following way: take the derivative with respect to  $t$  of the first equation in (39) and substitute  $\partial v_z^{0,0}/\partial t$  from the second equation to obtain

$$\begin{aligned} \frac{\partial^2 \eta^{0,0}}{\partial t^2} &= -\frac{1}{R} \frac{\partial}{\partial z} \int_0^R r \frac{\partial v_z^{0,0}}{\partial t} dr = -\frac{1}{\rho R} \frac{\partial}{\partial z} \int_0^R r \left( \mu \frac{1}{r} \frac{\partial}{\partial r} \left( r \frac{\partial v_z^{0,0}}{\partial r} \right) - \frac{\partial}{\partial z} (C \eta^{0,0}) \right) dr \\ &= -\frac{\mu}{\rho} \frac{\partial}{\partial z} \left( \frac{\partial v_z^{0,0}}{\partial r} \Big|_{r=R} \right) + \frac{RC}{2\rho} \frac{\partial^2 \eta^{0,0}}{\partial z^2} \end{aligned}$$

Therefore instead of (39), we solve the hyperbolic-parabolic system

$$\frac{\partial^2 \eta^{0,0}}{\partial t^2} - \frac{CR}{2\rho} \frac{\partial^2 \eta^{0,0}}{\partial z^2} = -\frac{\mu}{\rho} \frac{\partial}{\partial z} \left( \frac{\partial v_z^{0,0}}{\partial r} \Big|_{r=R} \right) \quad (50)$$

$$\rho \frac{\partial v_z^{0,0}}{\partial t} - \mu \frac{1}{r} \frac{\partial}{\partial r} \left( r \frac{\partial v_z^{0,0}}{\partial r} \right) = -C \frac{\partial \eta^{0,0}}{\partial z} \quad (51)$$

with the initial and boundary conditions (40). Perform the same computation for the 0, 1 approximation and replace (41) by

$$\frac{\partial^2 \eta^{0,1}}{\partial t^2} - \frac{CR}{2\rho} \frac{\partial^2 \eta^{0,1}}{\partial z^2} = -\frac{\mu}{\rho} \frac{\partial}{\partial z} \left( \frac{\partial v_z^{0,0}}{\partial r} \Big|_{r=R} \right) - \frac{1}{2R} \frac{\partial^2}{\partial t^2} (\eta^{0,0})^2 \quad (52)$$

$$\rho \frac{\partial v_z^{0,1}}{\partial t} - \mu \frac{1}{r} \frac{\partial}{\partial r} \left( r \frac{\partial v_z^{0,1}}{\partial r} \right) = -C \frac{\partial \eta^{0,1}}{\partial z} \quad (53)$$

with initial and boundary conditions given by (42).

The approximation 1, 0 is straightforward once the approximations 0, 0 and 0, 1 are obtained. The systems for the 0, 0 and 0, 1 approximations have the same form, with the mass and stiffness matrices equal for both problems, up to the boundary conditions. Thus they are generated only once. Solve them simultaneously using a time-iteration procedure. First solve the parabolic equation for  $v_z^{0,0}$  at the time step  $t_{i+1}$  by explicitly evaluating the right-hand side at the time-step  $t_i$ . Then solve the wave equation for  $\eta^{0,0}$  with the evaluation of the right-hand side at the time-step  $t_{i+1}$ . Using these results for  $v_z^{0,0}$  and  $\eta^{0,0}$ , computed at  $t_{i+1}$ , obtain a correction at  $t_{i+1}$  by repeating the process with the updated values of the right-hand sides. The numerical algorithm can be expressed:

### 1. Approximation 0, 0:

For  $i = 0$  to  $n_T$

(a) solve (51) at  $t_{i+1}$  for  $v_z^{0,0}$  using 1D FEM with linear elements and implicit time-discretization

(b) solve (50) at  $t_{i+1}$  for  $\eta^{0,0}$  using 1D FEM with  $C^1$  elements and implicit time-discretization

### 2. Approximation 0, 1:

For  $i = 0$  to  $n_T$

(a) solve (53) at  $t_{i+1}$  for  $v_z^{0,1}$  using 1D FEM with linear elements and implicit time-discretization

(b) solve (52) at  $t_{i+1}$  for  $\eta^{0,1}$  using 1D FEM with  $C^1$  elements and implicit time-discretization

### 3. Approximation 1, 0

(a) solve (48) for  $v_r^{1,0}$  using numerical integration

(b) solve (49) for  $v_z^{1,0}$  using 1D FEM with linear elements and implicit time-discretization

### 4. Compute the total approximation $v_r = v_r^{1,0}$ , $v_z = v_z^{0,0} + v_z^{0,1} + v_z^{1,0}$ , $\eta = \eta^{0,0} + \eta^{0,1}$ .

In this algorithm a sequence of 1D problems is solved, so the numerical complexity is that of 1D solvers. However, leading order two-dimensional effects are captured as shown in Figs. 6 and 7.

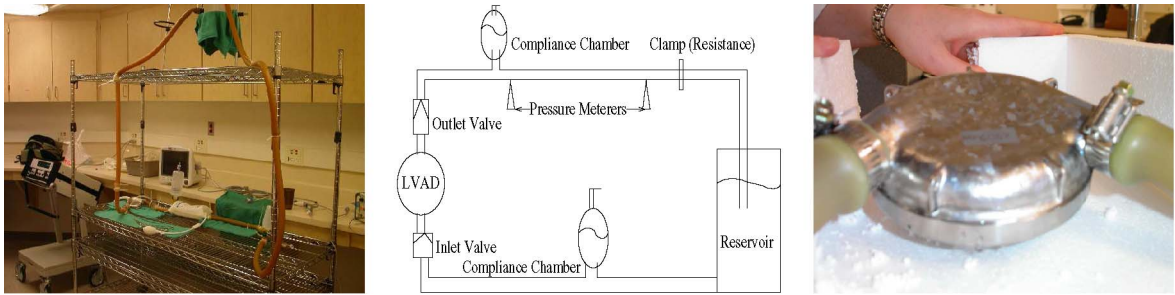


Fig. 3. Flow loop at the Cardiovascular Research Laboratory at the Texas Heart Institute (left), a sketch of the flow loop (middle) and a HeartMate Left Ventricular Assist Device (right).

Fig. 3. La boucle d'écoulement simulé au Cardiovascular Research Laboratory, Texas Heart Institute (à gauche), un croquis de la boucle d'écoulement simulé (au centre) et un HeartMate Left Ventricular Assist Device (à droite).

## 6. Numerical simulations and comparison with experiment

We used a mock circulatory loop to validate our mathematical flow model. Ultrasonic imaging and Doppler methods were used to measure axial velocity of the flow. Non-dairy coffee creamer was dispersed in water to enable reflection for ultrasound measurements. A high-frequency (20 MHz) single crystal probe was inserted through a catheter at several locations of the tube. In Fig. 4 right we show the results of the reading at the mid-point of the tube.

To determine the Young's modulus of the tube wall we measured the tube diameter  $d$  at the reference pressure of 84 mm Hg ( $d = 2.22$  cm) and at the maximal pressure of 148 mm Hg ( $d = 2.38$  cm), utilizing the linear pressure-displacement relationship (35) and the data for the tube wall thickness provided by the manufacturer of the latex tube Kent Elastomer Products Inc.

Fig. 3 shows the experimental set up, a sketch of the main components of the mock circulatory loop and the HeartMate Left Ventricular Assist Device used as pulsatile pump, typically inserted in patients to aid the function of the heart's left ventricle.

### 6.1. Comparison

Numerical simulations were performed for the flow loop parameter values, shown in Table 1, with the measured inlet and outlet pressure data shown in Fig. 4 left. A calculation of the non-dimensional parameter values shows that our model can be used to simulate the flow conditions in the experimental set up. More precisely, for the pressure data shown in Fig. 4 left, the value of the norm  $\mathcal{P}$  is around 15000, the average magnitude of the velocity  $V$ , defined in (21) is 0.68 m/s, the time scale parameter  $\omega = 30 \text{ s}^{-1}$ , and the Strouhal and Reynolds numbers defined in (28) and (29) are  $Sh = 15$ ,  $Re = 24$ ,  $Sh_0 = 0.5$  and  $Re_0 = 2247$ .

The axial component of the velocity measured at the mid-point of the tube (filtered data) was compared with the numerical simulation over one cardiac cycle. The two graphs, shown in Fig. 4 on the right, show excellent agreement indicating that the mathematical model we describe in this manuscript provides a good approximation for the flow.

Next we show the (two-dimensional) details of the simulations of the flow at four different times in the cardiac cycle. The subsequent figures show the radial (top subplot) and the axial (middle subplot) components of the velocity numerically calculated along the experimental tube superimposed over the streamlines of the flow. The color bars indicate the magnitude of the velocity in m/s. The bottom subplot shows the inlet pressure data in mm Hg with the red dot indicating the time in a cardiac cycle at which the corresponding snap-shots are taken. The displacement itself (not the entire radius) is magnified by a factor of five to emphasize the movement of the vessel wall. Notice how the radius of the tube changes as we progress in time from Fig. 5 left to Fig. 6 right. In Fig. 5 left the radius is roughly that of the configuration  $\Sigma_\varepsilon$ , with zero displacement and with the magnitude of the radial and axial components of the velocity near zero. Fig. 5 right captures the forward moving wave in the structure as the velocity increases at the beginning of the systole. The systolic peak is shown in Fig. 6 left. Notice the maximum displacement of the wall, as well as the fact that the axial component of the velocity dominates the flow (radial component of the velocity shown in the top subplot is zero). Finally, Fig. 6 right shows the end of systole and beginning of diastole. Notice the decrease

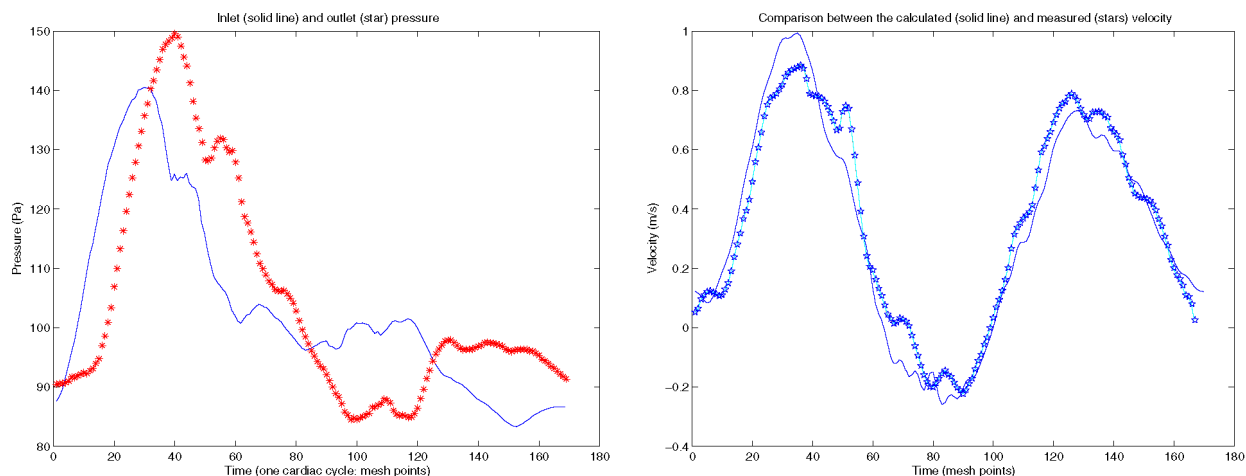


Fig. 4. The figure on the left shows the filtered inlet (solid line) and outlet (stars) pressure data measured experimentally. The figure on the right shows a comparison between the axial velocity measured experimentally (stars) and calculated numerically (solid line). The velocity is taken at the mid-point of the tube plotted as a function of time during one cardiac cycle.

Fig. 4. La figure à gauche montre les pressions à l'entrée (ligne solide) et à la sortie (étoiles), filtrées et mesurées expérimentalement. La figure à droite montre la comparaison entre la vitesse axiale, mesurée expérimentalement (étoiles) et calculée numériquement (ligne solide). Les valeurs de la vitesse, prises au milieu du tuyau, sont tracées comme une fonction du temps, pendant un cycle cardiaque.

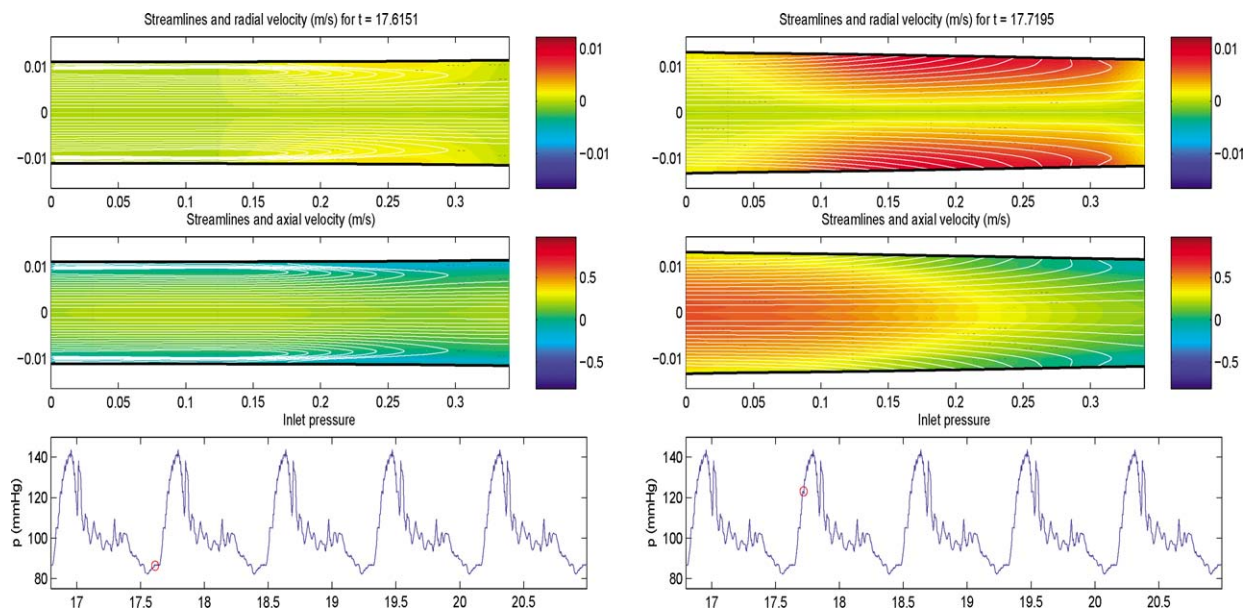


Fig. 5. The figure on the left corresponds to the snap-shot taken at diastole just before the inlet pressure begins to increase. The figure on the right corresponds to the snap-shot taken just before the systolic peak of the inlet pressure shown at the bottom subplot.

Fig. 5. La figure à gauche correspond à la photo prise à la diastole avant l'augmentation de la pression à l'entrée. La figure à droite correspond à la photo prise immédiatement avant le maximum systolique de la pression de l'entrée, montré sur sous-graph au fond.

in the radius and more pronounced secondary flows. All the figures clearly indicate two-dimensional features of the flow.

Fig. 7 right shows the radius versus tube length at the systolic peak, compared with the reference radius of  $R = 0.011$  m. Fig. 7 left presents the numerically calculated radial displacement over 25 cardiac cycles. Notice that its maximum value is just around the measured value of 0.8 mm.

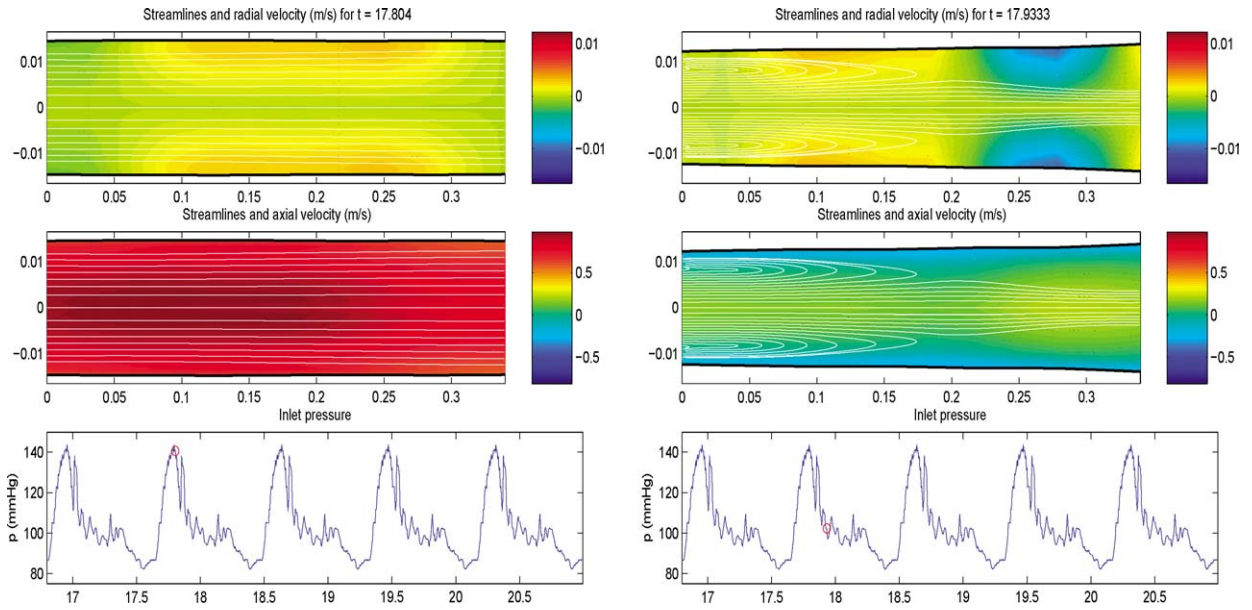


Fig. 6. The figure on the left shows the flow at systolic peak. The figure on the right shows the flow at the beginning of diastole.

Fig. 6. La figure à gauche montre l'écoulement au maximum systolique. La figure à droite montre l'écoulement au commencement de la diastole.

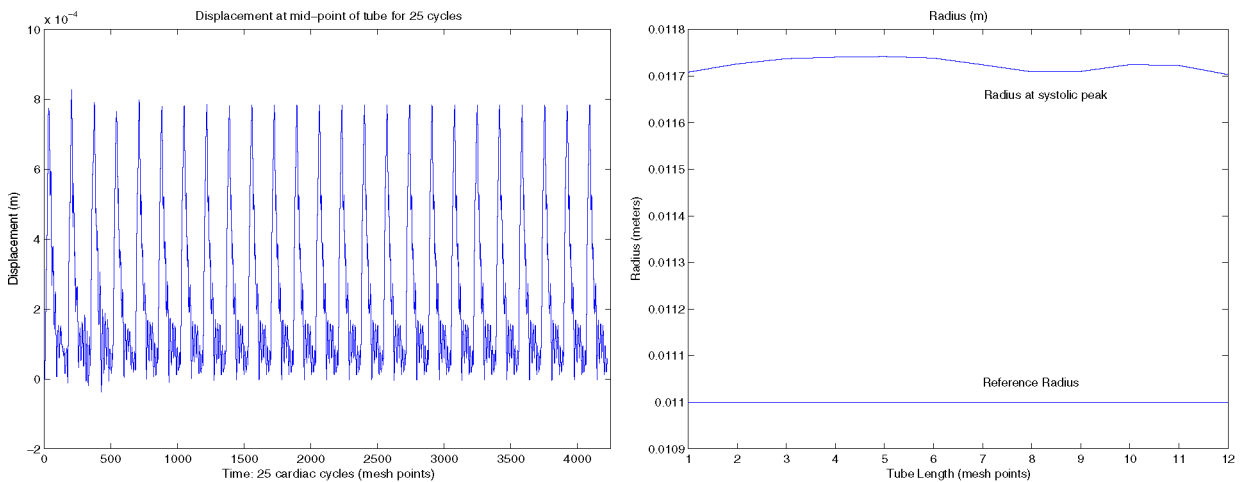


Fig. 7. The left subplot shows the numerically calculated displacement at the mid-point of the tube (axially and radially) for 25 cardiac cycles. The right subplot shows the reference radius and the radius at the systolic peak as a function of the tube length.

Fig. 7. Le sous-graph à gauche montre le déplacement, calculé numériquement, dans le point au milieu du tuyau (par l'axe et par le rayon) pour 25 cycles cardiaques. Le sous-graph à droite montre le rayon de référence et le rayon au maximum systolique comme une fonction de la longueur du tuyau.

## References

- [1] A. Quarteroni, M. Tuveri, A. Veneziani, Computational vascular fluid dynamics: problems, models and methods. Survey article, *Comput. Visual. Sci.* 2 (2000) 163–197.
- [2] W.W. Nichols, M.F. O'Rourke, *McDonald's Blood Flow in Arteries: Theoretical, Experimental and Clinical Principles*, fourth ed., Arnold and Oxford University.
- [3] R. Glowinski, T.W. Pan, J. Periaux, A fictitious domain method for Dirichlet problem and applications, *Comput. Methods Appl. Mech. Engrg.* 111 (3–4) (1994) 283–303.
- [4] R. Glowinski, Finite element methods for incompressible viscous flow, in: P.G. Ciarlet, J.L. Lions (Eds.), *Handbook of Numerical Analysis*, vol. IX, North-Holland, Amsterdam, 2003.



- [5] F. Nobile, Numerical approximation of fluid–structure interaction problems with application to haemodynamics, Ph.D. Thesis, EPFL, Lausanne, 2001.
- [6] K. Perktold, G. Rappitsch, Mathematical modeling of local arterial flow and vessel mechanics, in: J. Crolet, R. Ohayon (Eds.), *Computational Methods for Fluid Structure Interaction*, in: Pitman Res. Notes in Math., vol. 306, Longman, Harlow, 1994, pp. 230–245.
- [7] C.S. Peskin, D.M. McQueen, A three-dimensional computational method for blood flow in the heart – I. Immersed elastic fibers in a viscous incompressible fluid, *J. Comput. Phys.* 81 (2) (1989) 372–405.
- [8] A.M. Robertson, A. Sequeira, A director theory approach to modeling blood flow in the arterial system, *Math. Models Methods Appl. Sci.* 15 (2005) 871–906.
- [9] S. Čanić, E.-H. Kim, Mathematical analysis of the quasilinear effects in a hyperbolic model of blood flow through compliant axi-symmetric vessels, *Math. Methods Appl. Sci.* 26 (14) (2003) 1161–1186.
- [10] L. Formaggia, F. Nobile, A. Quarteroni, A one dimensional model for blood flow: application to vascular prosthesis, in: I. Babuska, T. Miyoshi, P.G. Ciarlet (Eds.), *Mathematical Modeling and Numerical Simulation in Continuum Mechanics*, in: Lect. Notes Comput. Sci. Eng., vol. 19, Springer, Berlin, 2002, pp. 137–153.
- [11] Y.C. Fung, *Biomechanics: Circulation*, second ed., Springer, New York, 1993.
- [12] M.S. Olufsen, C.S. Peskin, W.Y. Kim, E.M. Pedersen, A. Nadim, J. Larsen, Numerical simulation and experimental validation of blood flow in arteries with structured-tree outflow conditions, *Ann. Biomedical Engng.* 28 (2000) 1281–1299.
- [13] L. Formaggia, J.F. Gerbeau, F. Nobile, A. Quarteroni, On the coupling of 3D and 1D Navier–Stokes equations for flow problems in compliant vessels, *Comput. Methods Appl. Mech. Engrg.* 191 (2001) 561–582.
- [14] P.G. Ciarlet, *Mathematical Elasticity. Vol. III. Theory of Shells*, in: Stud. Math. Appl., vol. 29, North-Holland, Amsterdam.
- [15] P.G. Ciarlet, V. Lods, Asymptotic analysis of linearly elastic shells. I. Justification of membrane shell equations, *Arch. Rational Mech. Anal.* 136 (2) (1996) 119–161.
- [16] P.G. Ciarlet, V. Lods, Asymptotic analysis of linearly elastic shells. III. Justification of Koiter’s shell equations, *Arch. Rational Mech. Anal.* 136 (2) (1996) 191–200.
- [17] W.T. Koiter, On the foundations of the linear theory of thin elastic shells. I, II, *Nederl. Akad. Wetensch. Proc. Ser. B* 73 (1970) 169–182.
- [18] P. Luchini, M. Lupo, A. Pozzi, Unsteady Stokes flow in a distensible pipe, *Z. Angew. Math. Mech.* 71 (10) (1991) 367–378.
- [19] X. Ma, G.C. Lee, S.G. Wu, Numerical simulation for the propagation of nonlinear waves in arteries, *Trans. ASME* 114 (1992) 490–496.
- [20] S. Čanić, A. Mikelić, D. Lamponi, J. Tambača, Self-consistent effective equations modeling blood flow in medium-to-large compliant arteries, *SIAM J. Multisc. Anal. Simul.* 3 (2005) 559–596.
- [21] S. Čanić, A. Mikelić, Effective equations modeling the flow of a viscous incompressible fluid through a long elastic tube arising in the study of blood flow through small arteries, *SIAM J. Appl. Dynamical Systems* 2 (3) (2003) 431–463.
- [22] C. Chmielewsky, Master’s Thesis, North Carolina State University, 2004.
- [23] M.A. Biot, Theory of propagation of elastic waves in a fluid-saturated porous solid. I. Lower frequency range, *J. Acoust. Soc. Am.* 28 (2) (1956) 168–178;  
M.A. Biot, Theory of propagation of elastic waves in a fluid-saturated porous solid. II. Higher frequency range, *J. Acoust. Soc. Am.* 28 (2) (1956) 179–191.
- [24] J.-L. Auriault, Poroelastic media, in: U. Hornung (Ed.), *Homogenization and Porous Media*, in: Interdiscip. Appl. Math., Springer, Berlin, 1997, pp. 163–182.
- [25] E. Sanchez-Palencia, *Non-Homogeneous Media and Vibration Theory*, Lecture Notes in Phys., vol. 127, Springer, 1980.
- [26] A. Mikelić, in: M. Kirkilionis, S. Krömker, R. Rannacher, F. Tomi (Eds.), *Trends in Nonlinear Analysis*, Springer-Verlag, Heidelberg, 2002, pp. 225–267.
- [27] S. Čanić, A. Mikelić, Effective equations describing the flow of a viscous incompressible fluid through a long elastic tube, *C. R. Mecanique* 330 (2002) 661–666.